Lab on a Chip

PAPER

View Article Online
View Journal

Check for updates

Cite this: DOI: 10.1039/d5lc00992h

An active-matrix digital microfluidic device based on surfactant-mediated electro-dewetting

Xinying Xie, *[a] Qining Leo Wang, [b] Runxiao Shi,[a] Tengteng Lei,*[a] Chang-Jin "CJ" Kim [b] and Man Wong[a]

Received 23rd October 2025,
Accepted 16th January 2026

DOI: 10.1039/d5lc00992h

rsc.li/loc

Based on electrowetting mechanism, digital microfluidics (DMF) utilizes both direct-drive and active-matrix (AM) control of electrodes. Recently, DMF with surfactant-mediated electro-dewetting that electrically induces hydrophobic repulsion of droplets containing an ionic surfactant has also been demonstrated. However, existing electro-dewetting DMF devices are on a direct-drive controlled electrode array, which limits the number of independent electrodes. This work presents an AM electro-dewetting DMF device with continuous current to drive droplets. Indium–tin–zinc oxide top-gate self-aligned thin-film transistors are employed in the cell circuit to address and drive droplets with low voltage. The resulting AM electro-dewetting DMF devices are confirmed to transport, split, and merge droplets by using low voltage, opening the path for electro-dewetting DMF that offers a large number of independent electrodes.

Introduction

Microfluidics can be beneficially applied in life sciences,[1–6] chemical synthesis,[7,8] biological and chemical dynamic processes,[9,10] and thermodynamic issues.[11–13] It involves the manipulation of fluids in microscale environments and can be categorized into continuous flow-based and droplet-based microfluidics. As a subset of droplet-based microfluidics, digital microfluidics (DMF) manipulates discrete droplets individually and independently.[14–17] With unique reconfigurability, DMF facilitates the miniaturization and automation of diverse molecular biology and chemistry experiments, leading to significant reductions in both time and reagent costs.[16,17]

Currently, most DMF systems are realized with electrowetting-on-dielectric (EWOD) devices,[18,19] where a droplet is electrically attracted onto a hydrophobically coated surface with an apparent decrease of contact angle.[18,20–23] The contact angle decreased by 40° using 20–25 V actuation voltage in 0.05 seconds with a 100 nm silicon oxide layer as a dielectric layer and a 20 nm amorphous fluoropolymer as a hydrophobic layer.[21] On the EWOD device shown in Table 1, a droplet wets the electrode on the right side where it is attracted by the applied voltage, pulling itself to the right. However, the requirement of high voltages[24] and reliability issues such as electric charging[25,26] and dielectric breakdown[27,28] hinder wider adoption and commercialization of EWOD DMF.[17,19]

An alternative to EWOD, surfactant-mediated electro-dewetting[34] has recently been developed. Electro-dewetting-based DMF requires much lower actuation voltages and eliminates the need for dielectric and hydrophobic layers, thereby free of the reliability issues associated with the two layers.[41] Mechanistically opposite to electrowetting, which electrically attracts liquid on a hydrophobic surface, electro-dewetting electrically repels liquid on a hydrophilic surface. Ionic surfactant molecules present in the droplet are driven by an electric field and adsorbed on the hydrophilic substrate. The hydrophobic tails of the adsorbed surfactants render the surface more hydrophobic, thus increasing the contact angle of the droplet.[34,42,43] A sessile drop test for electro-dewetting was conducted on a bare silicon electrode with native oxide as a hydrophilic layer. The droplet used was deionized (DI) water containing 0.015 critical micelle concentration (CMC) of dodecyltrimethylammonium bromide (DTAB). The contact angle increased by 20° using only 3 V actuation voltage in 0.5 seconds.[34] Electro-dewetting exhibits a slower dynamic response, likely due to the time required for the migration and assembly of surfactant molecules, while the polarization of the dielectric layer in EWOD is nearly instantaneous.[34] Although the device operates without a top plate in ambient air, which requires consideration of droplet evaporation, several strategies can be employed to mitigate this issue, including oil encapsulation,[44] humidity control, and the use of low-volatility liquids.

---

[a] *The Hong Kong University of Science and Technology, Hong Kong. E-mail: xiexinying@ust.hk, eetlei@ust.hk*

[b] *University of California, Los Angeles, USA*

Table 1 Digital microfluidics devices based on EWOD or electro-dewetting and built on direct-drive or AM electrodes. Each of the direct-drive electrodes is connected directly to an independent channel of an external control circuit. Each of the AM electrodes is powered by its own set of transistors

Electrode addressing scheme	Liquid actuation mechanism	
	EWOD 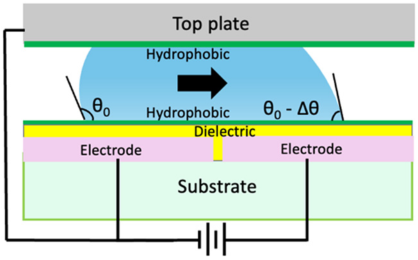 	Electyro-dewetting 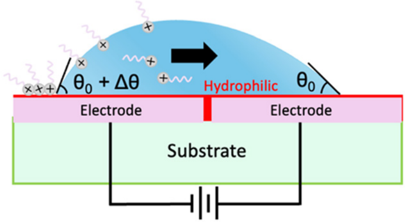
Direct-drive 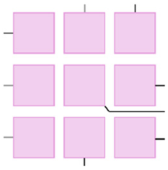	Direct-drive EWOD DMF[14,29–33]	Direct-drive electro-dewetting DMF[34,35]
AM 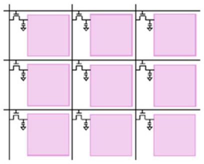	AM EWOD DMF[11,36–39]	AM electro-dewetting DMF[40], this work

On the electro-dewetting device shown in Table 1, a droplet dewets the electrode on the left side where the surfactant is absorbed by the applied voltage, pushing itself to the right. The surfactant concentration is commonly effective between 0.015 and 0.1 CMC. When the surfactant concentration is too low, there are insufficient molecules to significantly alter surface wettability. Conversely, if the concentration is too high, the contact angle may already be large before actuation, leaving little room for further increase.[34] The very low surfactant concentration used in electro-dewetting minimally affects droplet properties, and droplet generation, transportation, splitting, and merging were successfully achieved in a direct-drive device.[34]

To facilitate complex droplet operations essential for DMF devices, a substantial number of independently accessible electrodes are required, typically arranged in an $m \times n$ array on the device substrate as summarized in Table 1. Both EWOD[29–33] and electro-dewetting[34,35] devices utilize direct-drive control, which involves connecting each of the $m \times n$ electrodes (Table 1) to a dedicated external control circuit. However, this direct-drive approach, requiring $m \times n$ control lines, can lead to line interference and limit the number of electrodes.[45,46] In the case of EWOD, direct-drive control was introduced to allow $m + n$ control lines to drive the $m \times n$ electrodes[47] but presented with a limitation. This limitation has been overcome by adopting active-matrix (AM) control based on thin-film transistors (TFTs)[37,39,48–53] (Table 1). Unfortunately, the single-TFT cell circuit developed for EWOD DMF is not applicable to electro-dewetting DMF because unlike EWOD DMF, which requires a high voltage with no current, electro-dewetting DMF requires a small but continuous current with a low voltage.[34,41] Consequently, most cell circuit configurations for EWOD AM control[38,49,54,55] are not applicable to electro-dewetting DMF devices.

In this study, an AM electro-dewetting system is designed, constructed and characterized for DMF by deploying a unique cell circuit that supports continuous current. The cell circuits are realized using top-gate (TG) self-aligned (SA) amorphous metal oxide semiconductor (AMOS) indium–tin–zinc oxide (ITZO) TFTs, as AMOS TFTs have demonstrated superior performance, exhibiting enhanced device uniformity and lower costs compared to low-temperature polycrystalline silicon (LTPS) alternatives[56,57] and higher mobility than amorphous silicon (a-Si:H).[57] The most widely explored AMOS materials for TFT active layers are indium–gallium–zinc oxide (IGZO) and ITZO. ITZO TFTs exhibit a mobility approximately three times higher than that of IGZO TFTs and the higher mobility of the TFTs would allow a lower V_{DD} to actuate the droplet. Also, ITZO TFTs have already been successfully deployed in a 56 inch OLED TV. This demonstrates their suitability for large-scale production and reinforces their potential for widespread use in active matrix DMF devices.[57,58] Basic DMF operations, including droplet transport, splitting, and merging have been demonstrated at a reduced voltage of 25 V, compared to the >40 V[36,37,59] for common AM DMF systems based on EWOD as well as the 32 V used for the preliminary AM IGZO electro-dewetting device[40] that preceded this work.

Electro-dewetting

The commonly used source/drain (S/D) electrode material for ITZO TFTs is molybdenum (Mo) beneath aluminum (Al).[60,61] To determine the optimal experimental conditions for electro-dewetting with the above metal electrode and hydrophilic surface material for AM DMF devices, a sessile droplet test was used to characterize the contact-angle change induced by electro-dewetting, as schematically illustrated in Fig. 1A. The hydrophilic material applied is 30 nm SiO_x, thin enough to allow for currents, ensuring that it does not obstruct the current flowing through the droplet. A probe was used to contact the metal, while a platinum (Pt) wire with a diameter of 0.1 mm was inserted into the droplet. The contact angle was measured three times using a contact angle meter (Biolin Theta) at different positions under each condition. The effect of ionic surfactant concentration was studied first. Following the original paper on electro-dewetting by Li *et al.*,[34] the cationic surfactant DTAB was selected and tested under various concentrations in deionized (DI) water for electro-dewetting. As shown in Fig. 1B, the maximum contact-angle change was ~30° at 1/32 CMC under 5 V actuation voltage, while further increase of the DTAB concentration led to a drop of the contact-angle change. These results aligned with the previous findings on bare Si with native oxide.[34]

Various voltages were applied between the droplet and the substrate to find the optimal actuation voltage for electro-dewetting. As shown in Fig. 1C, 5 V induced a maximum contact-angle change of ~27° with 1/64 CMC DTAB and further increasing the voltage did not lead to a larger contact-angle change. Also, electrolysis and bubble formation were only observed at a high voltage of 7.5 V. At 5 V or below, any signs of electrolysis were not observed.

As shown in Fig. 1D, with 1/64 CMC DTAB and 5 V actuation voltage, the droplet exhibited a large contact-angle change (*i.e.*, ~27°) and a fast response speed (*i.e.*, <2 seconds).

Contact angles and the cross-sectional views of the droplets in the wetted (without actuation voltage) and dewetted (with 5 V actuation voltage) states are shown in Fig. 1E.

Cell design for AM electro-dewetting DMF

In a conventional 1-TFT-1-capacitor (1T1C) cell configuration (Fig. 2A), to achieve AM control, when a scan pulse is applied to activate the TFT, data is allowed to be transmitted to the S/D terminal and stored on the capacitor.[48,52] However, for an electro-dewetting DMF device, which does not have a dielectric layer, a droplet provides a conductive path for

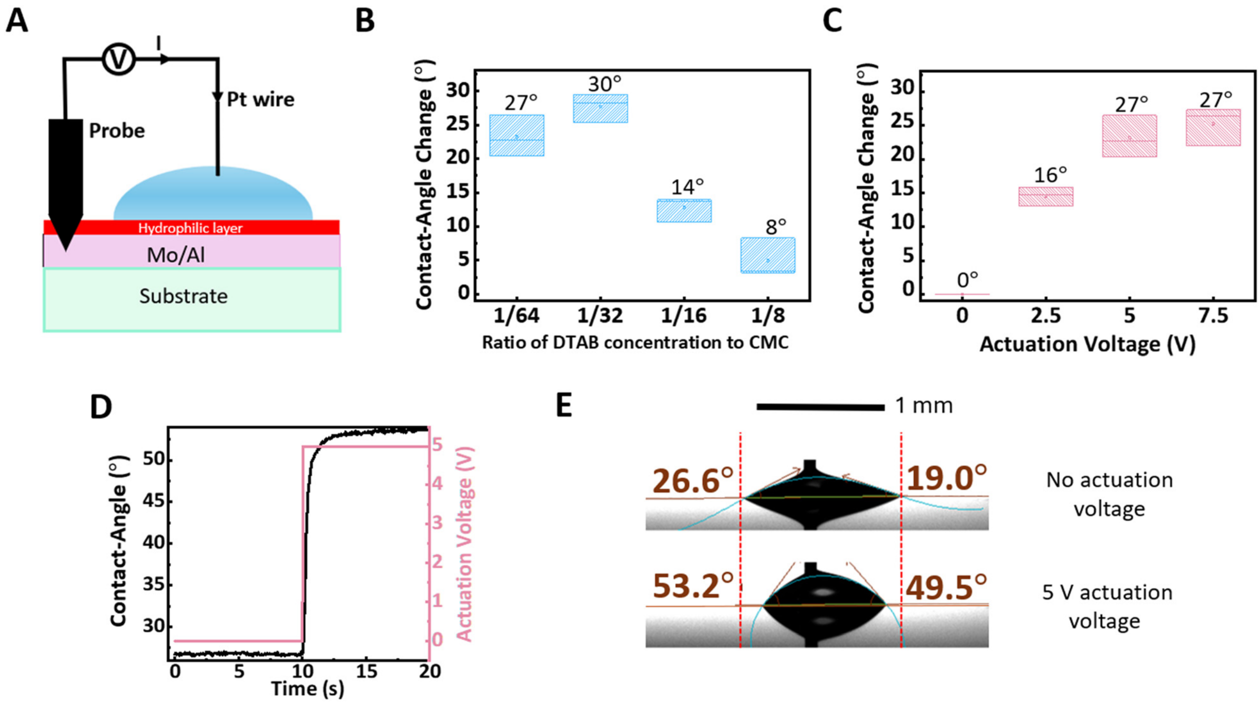

Fig. 1 (A) Experiment setup for electro-dewetting sessile droplet test. (B) Impact of DTAB concentrations (1/64, 1/32, 1/16, 1/8 CMC) on the change in contact angle induced by electro-dewetting, expressed as a ratio of concentration to critical micelle concentration (CMC). (C) Effect of actuation voltage on the electro-dewetting-induced change in contact angle, with applied voltages of 0, 2.5, 5, and 7.5 V, while the electrode remains grounded. (D) The response time of electro-dewetting-induced contact-angle change with 5 V actuation voltage. (E) Contact-angle change of DTAB-laden droplet when 5 V actuation voltage is applied.

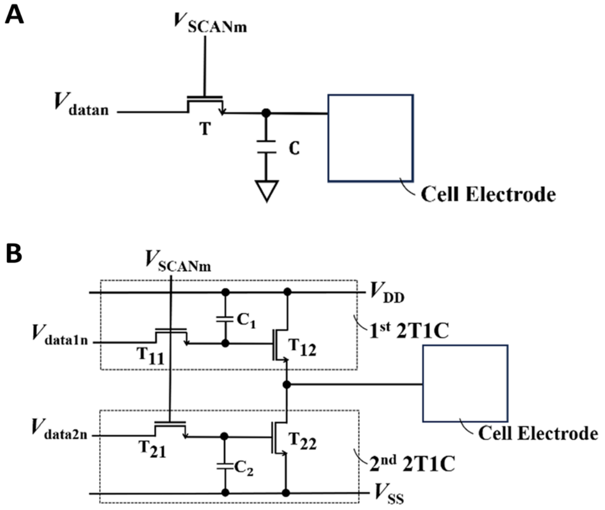

Fig. 2 Schematic cell circuit of (A) the conventional 1T1C configuration and (B) the designed 4T2C configuration for an AM electro-dewetting DMF device.

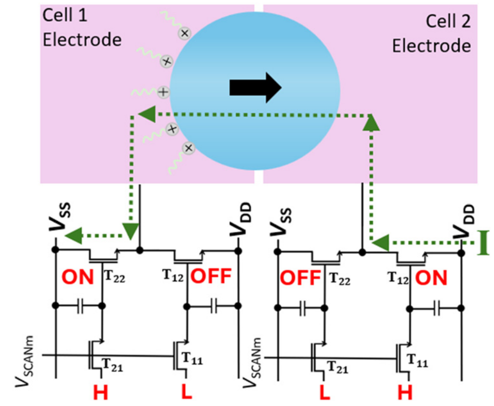

Fig. 3 Working principle of droplet transport in the AM electro-dewetting DMF device. The droplet containing DTAB spans two adjacent cell electrodes.

electric current to flow through it. Consequently, the capacitor in a traditional 1T1C cell circuit is unable to effectively store the charges to maintain a stable electric field for driving surfactant migration in electro-dewetting. See the simulation results with Fig. S1 in the SI.

The designed cell circuit consists of two identical 2-TFTs-1-capacitor (2T1C) sub-cell circuits, as illustrated in Fig. 2B. The 2T1C circuit includes the addressing TFTs T_{11} or T_{21}, the driving TFTs T_{12} or T_{22}, and the storage capacitors C_1 or C_2. The gate electrodes of T_{11} and T_{21} are connected to receive the scan signal ($V_{\mathrm{SCAN}m}$) for AM addressing. When the $V_{\mathrm{SCAN}m}$ is "high", the S/D terminals of T_{11} and T_{21} receive the data signals $V_{\mathrm{data1}n}$ and $V_{\mathrm{data2}n}$, respectively, which are stored on C_1 and C_2. When $V_{\mathrm{data1}n}$ is "high" and $V_{\mathrm{data2}n}$ is "low", T_{12} is turned on while T_{22} is turned off, and the cell electrode is connected to V_{DD} through T_{12} and placed in the "high" state. Conversely, when $V_{\mathrm{data1}n}$ is "low" and $V_{\mathrm{data2}n}$ is "high", T_{12} is turned off and T_{22} is turned on, and the cell electrode is connected to V_{SS} through T_{22} and placed in the "low" state. When $V_{\mathrm{data1}n}$ and $V_{\mathrm{data2}n}$ are both "low", T_{12} and T_{22} are both turned off, resulting in the cell electrode being disconnected from the power lines and placed in the "open" state.

As schematically illustrated in Fig. 3, the electrode in cell 2 is "high" and connected to V_{DD} through T_{12}, while the electrode in cell 1 is connected to V_{SS} through T_{22}. A current flows from V_{DD} through T_{12} in cell 2, the droplet, T_{22} in cell 1, and finally to V_{SS}. When a positively charged cationic surfactant such as DTAB is used, DTAB molecules will be driven to migrate towards V_{SS} in cell 1, causing the droplet to move towards cell 2.

The driving TFTs T_{12} in cell 2 and T_{22} in cell 1 regulate current magnitude. Thus, a lower resistance of the driving TFTs would allow a lower V_{DD} to actuate the droplet. Consequently, higher mobility of the active layer in the TFTs will decrease TFT resistance. Also, the width (W) was increased to 20 μm to decrease TFT resistance. Simultaneously, a length (L) of 10 μm was maintained to prevent short-channel effects.

To set the cell electrode state at the (m, n) cell point in the AM, the data signals ($V_{\mathrm{data1}n}$ and $V_{\mathrm{data2}n}$) for the nth column are applied to the S/D of addressing transistors when scan pulse $V_{\mathrm{SCAN}m}$ is "high" to turn on the addressing transistor at the mth row. The data signals ($V_{\mathrm{data1}n}$ and $V_{\mathrm{data2}n}$) for the nth column are then stored on the capacitors at the (m, n) cell point. When $V_{\mathrm{SCAN}m}$ transitions to "low", the addressing transistor at the mth row are turned off. The stored data on the capacitor which controls the driving transistor, will remain at the desired level until the next time when $V_{\mathrm{SCAN}m}$ is "high".

The simulation of node potential and the current across the droplet in a 4T2C configuration for a 2 × 1 AM electro-dewetting application AM operation are illustrated in Fig. S2 in the SI. This configuration allows the current to be sustained across the droplet during the electro-dewetting operation.

The storage capacitors are 3 pF. As shown in Fig. S3 in the SI, the discharging time from 20 to 0 V is significantly faster, at ~5 μs, while the charging time to increase from 0 to 20 V is ~47 μs. To ensure adequate charging, the scan signal pulse width was set to 200 μs, which exceeds the minimum required width of 50 μs. The 3 pF capacitor provides ample charge storage capacity, maintaining stable gate voltages for the ITZO driving TFT, with a gate current of approximately 1 pA during operation. The cell circuit configuration allows the capacitor to hold the necessary charge to sustain the gate voltage over time without significant droop. Consequently, the voltage at the electrode effectively follows the charging and discharging of the voltage on storage capacitor, ensuring reliable actuation.

To turn off addressing TFTs (*i.e.*, T_{11} and T_{21}), $V_{\mathrm{SCAN}m}$ should be set low. The V_{gs} for T_{11} and T_{21} given by $V_{\mathrm{gs}} = V_{\mathrm{SCAN}m} - V_{\mathrm{data1}n}$ and $V_{\mathrm{gs}} = V_{\mathrm{SCAN}m} - V_{\mathrm{data2}n}$, respectively, must be smaller than the turn on voltage (V_{on}) of both T_{11} and T_{21}. V_{on} is defined as the V_{g} needed to generate an I_{d} = 10 pA. For a low level of $V_{\mathrm{SCAN}m}$ set to be 0 V, the low level of $V_{\mathrm{data1}n}$ and $V_{\mathrm{data2}n}$ are set to be 3.3 V to ensure T_{11} and T_{21} are fully turned off when $V_{\mathrm{SCAN}m}$ is "low". Therefore, the range of $V_{\mathrm{SCAN}m}$ is 0 V–V_{DD}, while the range for $V_{\mathrm{data1}n}$ and $V_{\mathrm{data2}n}$ is 3.3 V–V_{DD}.

To turn off driving TFTs T_{12} and T_{22}, the $V_{\mathrm{data1}n}$ and $V_{\mathrm{data2}n}$ should be "low" (3.3 V). The V_{gs} for T_{11} and T_{21} given by V_{gs} = 3.3 V − V_{SS} and V_{gs} = 3.3 V − V_{SS} of T_{22}, respectively, must also be smaller than the V_{on} of T_{12} and T_{22}. Consequently, V_{SS} is set to be 8 V to ensure that both T_{12} and T_{22} can be fully turned off.

Fabrication of AM electro-dewetting DMF device

As shown in Fig. 4, the fabrication process began with the sputtering and patterning of a 150 nm molybdenum (Mo) layer on oxidized Si substrate as the data lines for inputting $V_{\mathrm{data1}n}$ and $V_{\mathrm{data2}n}$ as well as one electrode of the storage capacitor (CE1). 50 nm SiN_y dielectric was subsequently deposited. Next, 100 nm SiO_x was deposited. This $\mathrm{SiO}_x/\mathrm{SiN}_y$ stack serves as the 1st interlayer dielectric layer (ILD1) (Fig. 4A). Then, 25 nm ITZO was deposited and patterned as the active layer for both TFTs in the 2T1C circuit and the second electrode of the storage capacitor (CE2). The 100 nm SiO_x layer was then formed as the gate insulator (GI). A "post-GI" furnace anneal was performed in O_2 to oxidize the active layer and eliminate defects at the interface between the GI and the active layer (Fig. 4B). Following this, 150 nm Mo was sputtered and patterned to serve as the TG of the TFTs and the scan line for inputting $V_{\mathrm{SCAN}m}$. The 200 nm SiO_x layer as the 2nd interlayer dielectric layer (ILD2) was subsequently deposited (Fig. 4C), followed by annealing in O_2. SA S/D regions of the TFTs were then formed (Fig. 4D). 300 nm SiO_x was subsequently deposited using PECVD as the 3rd interlayer dielectric layer (ILD3) to repair the damage from SA S/D formation (Fig. 4E). Contact holes were then opened (Fig. 4F). Next, stacks of 300 nm Mo beneath 400 nm titanium (Ti) were sputtered and patterned to form the connections and the cell electrode (Fig. 4G). Ti was used as it offers superior stability during the electro-dewetting process, whereas other conductive materials that are more chemically active, such as aluminum (Al), can be damaged under similar conditions. 200 nm SiO_x was then deposited as the 4th interlayer dielectric layer (ILD4) isolating the Mo/Ti connection lines from the droplet (Fig. 4H). The cell electrodes were then exposed. Finally, a hydrophilic layer was deposited using 30 nm SiO_x (Fig. 4I), thin enough for current flowing through the droplet and compatible with the TFT fabrication process.

The 8 × 8 AM arrays have been constructed based on the above fabrication process, as illustrated in Fig. 5A. The arrays feature a cell size of 2 mm × 2 mm (Fig. 5B), with the cell circuits shown in Fig. 5C.

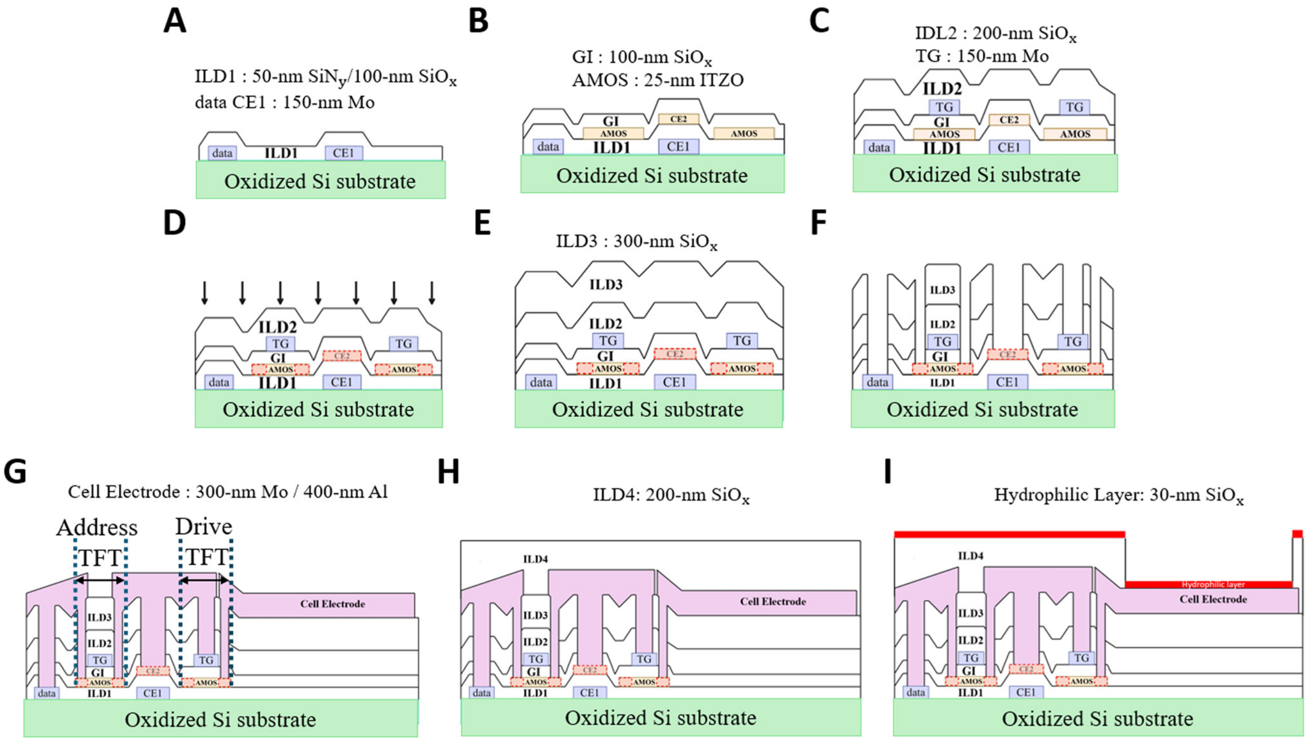

Fig. 4 Microfabrication process of the electro-dewetting DMF device integrated with the AM of TG SA ITZO TFT: (A) sputtering and patterning of Mo as data lines and CE1, followed by deposition of ILD1; (B) deposition and patterning of the active layer for both TFTs in the 2T1C-circuit and CE2, followed by deposition of GI; (C) sputtering and patterning of Mo as TG and scan lines, followed by deposition of ILD2; (D) S/D activation; (E) deposition of ILD3; (F) opening of contact hole; (G) sputtering and patterning of the Mo/Ti stack to form the connection and cell electrode; (H) deposition of ILD4; (I) exposure of the cell electrode, followed by deposition of the hydrophilic layer.

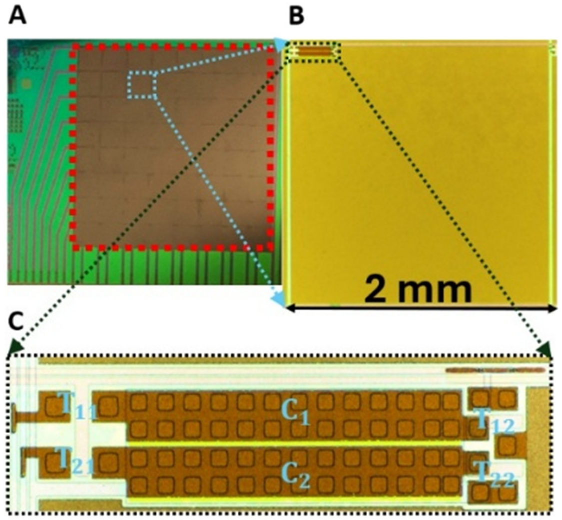

Fig. 5 Pictures of (A) the 8 × 8 AM array for electro-dewetting, (B) its cell and (C) its cell circuit.

ITZO TFT performance

To evaluate the stability of ITZO TFTs under current stress, the device was subjected to V_{gs} = 15 V and V_{ds} = 5 V to simulate ITZO TFT under electro-dewetting operation. The evolution of the transfer characteristics is shown in Fig. 6. Notably, the ITZO TFTs maintained consistent performance even after 1000 s of current stress.

The I_d *vs.* V_g transfer characteristics at V_d = 0.5 V and 5 V of TG SA ITZO TFTs with W/L = 10/10 μm (addressing TFTs) and W/L = 20/10 μm (driving TFTs) were measured at 15 different positions across a 4 inch wafer, as presented in Fig. 7. The position numbers on the wafer are shown in the inset of the transfer characteristics. The performances of the TFTs are largely uniform across the wafer.

The ITZO TFTs with above fabrication process have exhibited good repeatability across the past four years.[62–65] The electronic parameters of ITZO TFTs with W/L = 10/0 μm and 10/20 μm are summarized in Table 2, extracted from the TFTs respectively at a low V_d = 0.5 V. The field-effect mobility is calculated as $\mu_{FE} \equiv Lg_m/(WC_iV_d)$, where g_m is the maximum transconductance and C_i is the gate capacitance per unit area. The sub-threshold slope (SS) is extracted from the minimum value of $\partial \log I_d/\partial V_g$ for $V_g > V_{on}$.

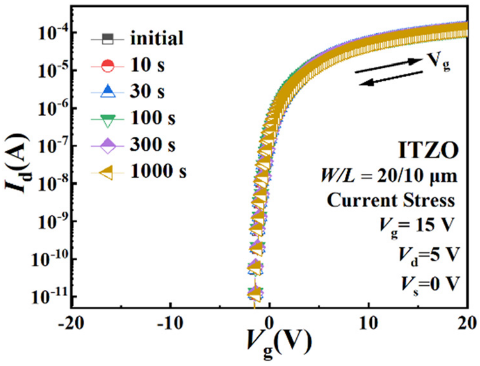

Fig. 6 The evolution of I_d *vs.* V_g transfer characteristics with current stress time.

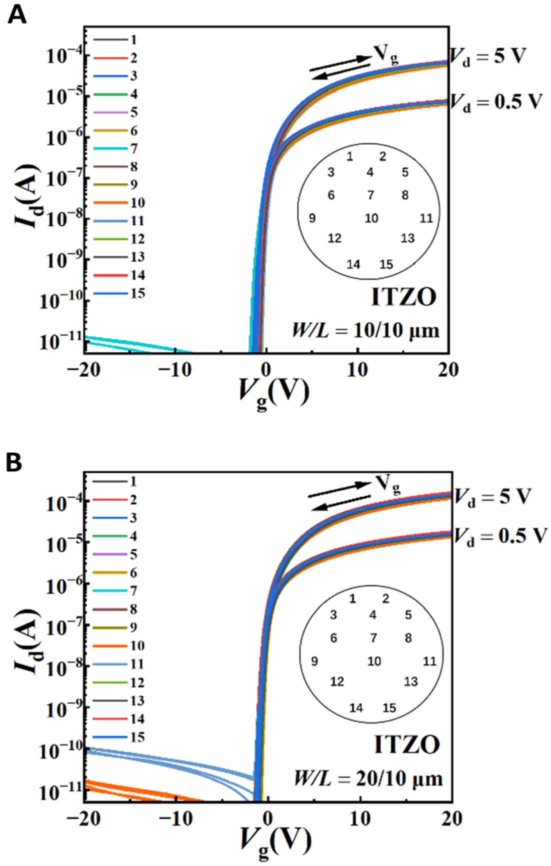

Fig. 7 The transfer characteristics of TFTs of (A) W/L = 10/10 μm and (B) W/L = 20/10 μm at different positions of the wafer. The position numbers on the wafer are shown in the insets.

Table 2 The electronic parameters of ITZO TFTs with W/L = 10/10 μm and 10/20 μm

W/L (μm)	μ_{FE} (cm^2 V^{-1} s^{-1})	SS (mV dec^{-1})	V_{on} (V) (V_g@I_d = 1 pA)	I_{off} (A)
10/10	~40	~225	−0.16–−0.8	$<10^{-11}$
20/10	~40	~200	−0.14–−0.8	$<10^{-10}$

Experiments for DMF operation and discussion

To assess the droplet manipulation capability of the developed AM electro-dewetting DMF device, a series of experiments for basic DMF operations was performed. As schematically illustrated in Fig. 8, the experiment setup included a computer that runs a LabView program as the graphical user interface, a microcontroller, a driver board powered by a DC voltage supply, and the AM electro-dewetting chip connected with the driver circuit through a flexible printed circuit (FPC).

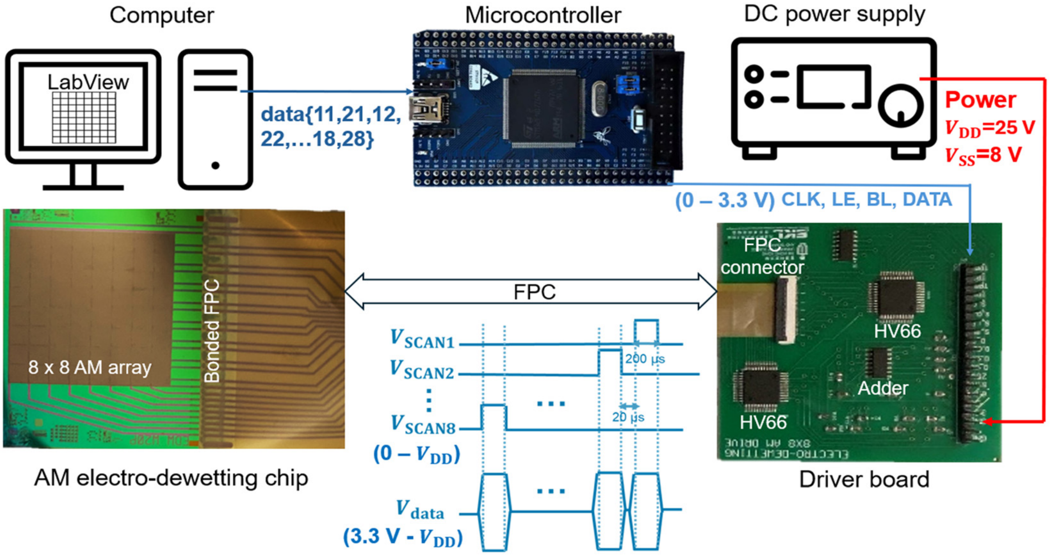

Fig. 8 Experiment setup to control the AM electro-dewetting chip for DMF operations.

The cell electrode states ("high", "low", or "open") within the array are set using LabVIEW, which packs the corresponding $V_{\text{data}1n}$ and $V_{\text{data}2n}$ for each cell and sends the data pack to the microcontroller (STM32F407ZG). The microcontroller controls HV66 on the driver board, a low-voltage serial to high-voltage parallel converter, to output $V_{\text{SCAN}m}$ ranging from 0 V to V_{DD}. This is achieved by generating data, clock (CLK), latch enable (LE) and blank (BL) signals (0–3.3 V) for the HV66. The microcontroller controls another HV66 to output $V_{\text{data}1n}$ and $V_{\text{data}2n}$ from 3.3 V to V_{DD} by using an adder circuit to raise the input signals (0–3.3 V) from the microcontroller to a range spanning from 3.3 V to 6.6 V.

Basic DMF droplet operations for the AM electro-dewetting device such as transporting, splitting, and merging were demonstrated, as highlighted in Fig. 9. As shown in Fig. 9A, a DI water droplet containing 1/64 CMC DTAB, with its pH adjusted to 4.5 to alleviate "autophobing",[66,67] was placed on the AM electro-dewetting device. As shown in Fig. 9B, the rear end of the droplet was repelled to retract. Note that since a cationic surfactant was used, any electrode actuated as "low" will attract those surfactant molecules and repel the droplet. To drive the droplet to move along a desired pathway, we applied "low" voltage to the electrodes surrounding the droplet pathway, which constantly repels and confines the droplet during transporting. As shown in Fig. 9B–F, all electrodes in front of the droplet were constantly actuated to be "high" during the transporting process. This was to ensure that those electrodes in front of the droplet never repel it regardless of how many electrodes the droplet spans across during movement. This extra caution was taken since the inactivated electrode can connect to the activated electrodes through the droplet, which may disrupt the intended transport path to move forward depending on the droplet shape. This interaction can lead to unintended repulsion or attraction forces that affect the droplet movement. To mitigate this issue, it is essential to maintain a stable voltage on the electrodes. By applying a "high" voltage on the electrodes in the intended transport path, the droplet path can be well controlled. Satellite droplets are observed during transportation in Fig. 9E and F. This can indeed introduce contamination and present challenges during droplet transportation. One effective approach to address this issue is to enhance the surface smoothness of the electrodes. Currently, the droplet must "climb" over the "hill" formed by the ILD4 layer situated between adjacent cell electrodes, as shown in Fig. 4I. A potential mitigation strategy is to improve the fabrication process to enhance the flatness of the surface. For example, cell electrodes may be deposited after the ILD4 layer to reduce the "hill". The average speed of transportation is 0.15 mm s^{-1}.

As shown in Fig. 9G–I, droplet splitting was demonstrated on the electro-dewetting DMF device. Distinct from the droplet actuation scheme for transporting, the actuation scheme for droplet splitting does not need to confine the droplet since it is desirable to let the left and right edges of the droplet spread in various directions during splitting. Therefore, only a column of electrodes was actuated to be "low" so that liquid on these electrodes was repelled to retract and eventually pinched off, as shown in Fig. 9H and I. The time taken to split the droplet into two droplets separated by 2 mm was about 6 seconds.

Droplet merging was also demonstrated by using a similar actuation scheme to that for droplet transport, as shown in Fig. 9J–L. Merging of two droplets initially separated by 4 mm took around 15 seconds.

The cell-level specifications are summarized in Table 3.

Compared in Table 4 are the AM DMF device in this work and other AM DMF devices in the literature. Compared to the

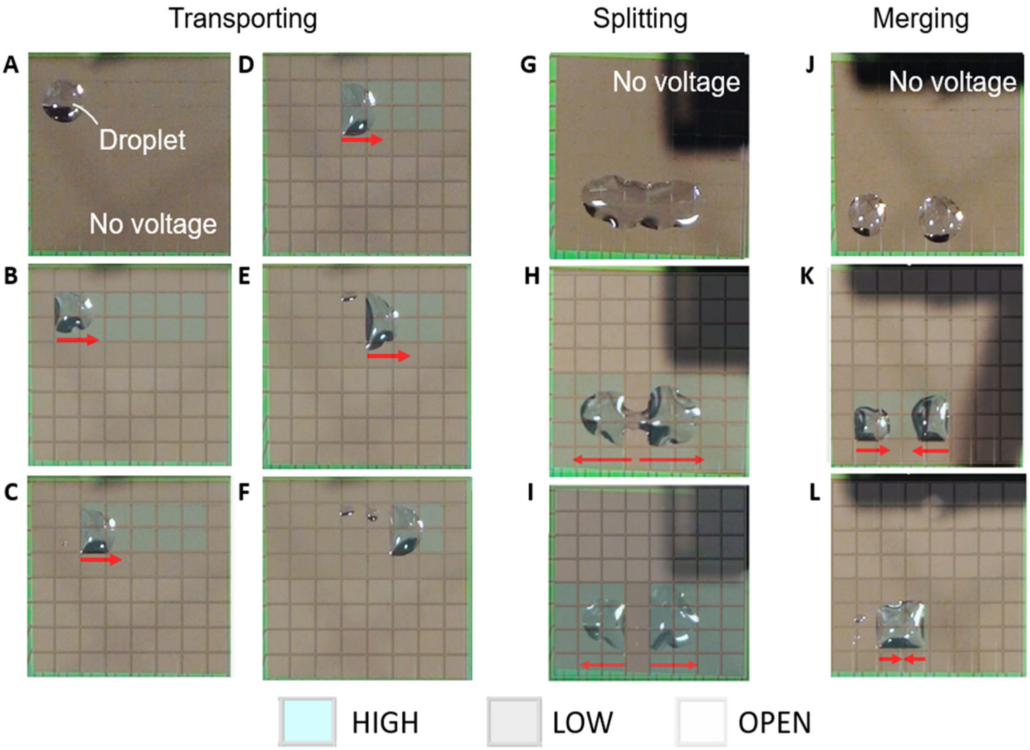

Fig. 9 Basic droplet operations and corresponding actuation scheme. The actuation state for each electrode is indicated by colour, *i.e.*, blue for “high”, grey for “low”, and white for “open”. The schematic pictures of actuation schemes for the 8 × 8 array are made transparent and are overlaid with pictures of droplet operations to indicate the actuation states for each step and each electrode during the droplet operation process. (A–F) Droplet pictures and corresponding actuation scheme for droplet transport. (G–I) Droplet pictures and corresponding actuation scheme for droplet splitting. (J–L) Droplet pictures and corresponding actuation for droplet merging.

Table 3 Cell-level specifications

Cell size (mm^2)	V_{DD} (V)	V_{SS} (V)	Addressing TFTs (*W*/*L*)	Driving TFTs (*W*/*L*)
2 × 2	25	8	10/10 μm	20/10 μm

AM EWOD device, the speed of the AM electro-dewetting device is slower. However, the lower actuation voltage required for electro-dewetting allowed for reduced voltage of both data and scan signals. Furthermore, the higher mobility of ITZO TFTs (~40 cm^2 V^{-1} s^{-1}) compared to IGZO TFTs (~16.6 cm^2 V^{-1} s^{-1})[68] further enabled lower voltage signals compared to our previous work. It is worth noting that despite the very low concentration (*i.e.*, <1/10 CMC), the reliance on ionic surfactant of electro-dewetting may pose challenges for specific bioassays involving living cells. For biochemical applications, further characterization is necessary to assess the compatibility of the ionic surfactant with the reagents used.

Conclusion

An AM electro-dewetting DMF device with an 8 × 8 AM array has been designed, fabricated, and demonstrated for basic droplet operations, addressing the limitations posed by direct-drive control for DMF. By utilizing a 4T2C cell circuit, continuous current was achieved to drive droplets by the mechanism of surfactant-mediated electro-dewetting. The

Table 4 Comparison of the AM DMF device

	DMF device	Active layer	Cell circuit	V_{SCAN} (V)	V_{data} (V)	Droplet speed (mm s^{-1})
This work	Electro-dewetting	ITZO	4T2C	0–25	3.3–25	0.15
40	Electro-dewetting	IGZO	4T2C	0–32	3.3–32	0.04
1	EWOD	Not known	1T1C	0–50	0–40	Not known
11	EWOD	IGZO	1T1C	0–35	0–31	6
48	EWOD	a-Si	1T1C	0–45	0–35	5
50	EWOD	a-Si	3T1C	0–40	0–35	Not known
55	EWOD	IGZO	5T1C	0–45	0–40	Not known

maximum voltage required for the AM electro-dewetting device is only 25 V, which is lower than that of typical AM EWOD DMF devices. By eliminating the need for dielectric and hydrophobic layers, the AM electro-dewetting device paves the way for more reliable AM DMF systems, making it suitable for a diverse range of lab-on-a-chip applications. While the proof-of-concept device for active-matrix electro-dewetting has been demonstrated, system-level performances such as device lifetime, droplet volume consistency, and parallel multi-droplet operation have not been extensively characterized. It is acknowledged that further investigation should be conducted to address these limitations.

Author contributions

C.-J. K. and M. W. conceived and initiated the research. X. X. designed the layout, developed the fabrication process, fabricated the device, wrote the code for microcontroller, programmed LabView, designed PCB board and conducted the experiment. X. X., Q. L. W. and R. S. discussed the experiment and fabrication process. X. X., R. S., T. L. and M. W. discussed the cell circuit. M. W., Q. L. W. and C.-J. K. revised the manuscript. M. W. supervised the research. All authors discussed the results and commented on the manuscript.

Conflicts of interest

The authors declare no conflict of interest.

Data availability

The 1T1C and 4T2C cell circuit configuration simulation for electro-dewetting as well as 2T1C configuration simulation for capacitor charging and discharging time have been included in the supplementary information (SI).

The droplet movement video can be found at Supplementary movie.

The program for LabVIEW can be found at https://1drv.ms/u/c/5c4b56d934f80dd3/IQBhozignIfHR7RQfkMlbiSdATXgSyNcO4bt9NL4HzL1yNY?e=MlpyUU. The version of the code employed for this study is LabVIEW 2018.

The code for microcontroller (STM32F407ZG) can be found at https://1drv.ms/f/c/5c4b56d934f80dd3/IgAYNkHhnFkUQZutVqrId_JDAVKpL2PKCJ3t7v3S_G90IvM?e=ERrnVZ. The version of the code employed for this study is MDK 5.

Supplementary information is available. See DOI: https://doi.org/10.1039/d5lc00992h.

Acknowledgements

The devices were fabricated at The Nanosystem Fabrication Facility (NFF) of The Hong Kong University of Science and Technology. Q. L. W. and C.-J. K. were partially supported by the National Science Foundation (1711708).

References

1 S. Hu, J. Ye, S. Shi, C. Yang, K. Jin, C. Hu, D. Wang and H. Ma, Large-area electronics-enabled high-resolution digital microfluidics for parallel single-cell manipulation, *Anal. Chem.*, 2023, **95**(17), 6905–6914.
2 A. M. Streets and Y. Huang, Chip in a lab: Microfluidics for next generation life science research, *Biomicrofluidics*, 2013, **7**(1), 011302.
3 J. Wu, H. Fang, J. Zhang and S. Yan, Modular microfluidics for life sciences, *J. Nanobiotechnol.*, 2023, **21**(1), 85.
4 K. Jiang, C. Dong, Y. Xu and L. Wang, Microfluidic-based biomimetic models for life science research, *RSC Adv.*, 2016, **6**(32), 26863–26873.
5 T. Adam, U. Hashim and K. Foo, Microfluidics design and fabrication for life sciences application, *Adv. Sci. Lett.*, 2013, **19**(1), 48–53.
6 B. Xiong, K. Ren, Y. Shu, Y. Chen, B. Shen and H. Wu, Recent developments in microfluidics for cell studies, *Adv. Mater.*, 2014, **26**(31), 5525–5532.
7 Y. Xing, Y. Liu, R. Chen, Y. Li, C. Zhang, Y. Jiang, Y. Lu, B. Lin, P. Chen, R. Tian, X. Liu and X. Cheng, A robust and scalable active-matrix driven digital microfluidic platform based on printed-circuit board technology, *Lab Chip*, 2021, **21**(10), 1886–1896.
8 H. Van Nguyen, K. Y. Kim, H. Nam, S. Y. Lee, T. Yu and T. S. Seo, Centrifugal microfluidic device for the high-throughput synthesis of Pd@ AuPt core-shell nanoparticles to evaluate the performance of hydrogen peroxide generation, *Lab Chip*, 2020, **20**(18), 3293–3301.
9 D. N. Breslauer, P. J. Lee and L. P. Lee, Microfluidics-based systems biology, *Mol. BioSyst.*, 2006, **2**(2), 97–112.
10 O. J. Dressler, X. Casadevall i Solvas and A. J. DeMello, Chemical and biological dynamics using droplet-based microfluidics, *Annu. Rev. Anal. Chem.*, 2017, **10**, 1–24.
11 J. H. Noh, J. Noh, E. Kreit, J. Heikenfeld and P. D. Rack, Toward active-matrix lab-on-a-chip: programmable electrofluidic control enabled by arrayed oxide thin film transistors, *Lab Chip*, 2012, **12**(2), 353–360.
12 B. Pinho, S. Girardon, F. Bazer-Bachi, G. Bergeot, S. Marre and C. Aymonier, A microfluidic approach for investigating multicomponent system thermodynamics at high pressures and temperatures, *Lab Chip*, 2014, **14**(19), 3843–3849.
13 S. Sevim, A. Sorrenti, C. Franco, S. Furukawa, S. Pané, A. J. deMello and J. Puigmartí-Luis, Self-assembled materials and supramolecular chemistry within microfluidic environments: from common thermodynamic states to non-equilibrium structures, *Chem. Soc. Rev.*, 2018, **47**(11), 3788–3803.
14 S. K. Cho, H. Moon and C.-J. Kim, Creating, transporting, cutting, and merging liquid droplets by electrowetting-based actuation for digital microfluidic circuits, *J. Microelectromech. Syst.*, 2003, **12**(1), 70–80.
15 K. Choi, A. H. Ng, R. Fobel and A. R. Wheeler, Digital microfluidics, *Annu. Rev. Anal. Chem.*, 2012, **5**(1), 413–440.

16 Y. Xu, W. Wu, Z. Zhou, Q. Su, X. Liu and W. Li, *et al.*, Digital Microfluidic Lab-on-a-Chip on a TFT Glass Substrate Enabling Point-of-Care Testing, *IEEE Electron Device Lett.*, 2023, 1500–1503.

17 J. Li and C.-J. Kim, Current commercialization status of electrowetting-on-dielectric (EWOD) digital microfluidics, *Lab Chip*, 2020, **20**(10), 1705–1712.

18 J. Lee, H. Moon, J. Fowler, T. Schoellhammer and C.-J. Kim, Electrowetting and electrowetting-on-dielectric for microscale liquid handling, *Sens. Actuators, A*, 2002, **95**(2–3), 259–268.

19 Q. L. Wang, E. H. Cho, J. Li, H. C. Huang, S. Kin, Y. Piao, L. Xu, K. Tang, S. Kuiry, Z. He, D. Yu, B. Cheng, C. C. Wu, C. Choi, K. Shin, T. Y. Ho and C.-J. Kim, Democratizing digital microfluidics by a cloud-based design and manufacturing platform, *Lab Chip*, 2024, **24**(19), 4536–4548.

20 H. Ren, R. B. Fair and M. G. Pollack, Automated on-chip droplet dispensing with volume control by electro-wetting actuation and capacitance metering, *Sens. Actuators, B*, 2004, **98**(2–3), 319–327.

21 H. Moon, S. K. Cho, R. L. Garrell and C.-J. Kim, Low voltage electrowetting-on-dielectric, *J. Appl. Phys.*, 2002, **92**(7), 4080–4087.

22 F. Mugele and J. Buehrle, Equilibrium drop surface profiles in electric fields, *J. Phys.: Condens. Matter*, 2007, **19**(37), 375112.

23 W. C. Nelson and C.-J. Kim, Droplet actuation by electrowetting-on-dielectric (EWOD): A review, *J. Adhes. Sci. Technol.*, 2012, **26**(12–17), 1747–1771.

24 Q. L. Wang, J. Li, H. S. E. Cho, L. Xu, A. Wang and S. Kuiry, *International Conference on Micro Electro Mechanical Systems (MEMS)*, Austin, TX, USA, 2024.

25 D. Thomas, M. C. Audry, R. M. Thibaut, P. Kleimann, F. Chassagneux, M. Maillard and A. Brioude, Charge injection in dielectric films during electrowetting actuation under direct current voltage, *Thin Solid Films*, 2015, **590**, 224–229.

26 B. Koo and C.-J. Kim, Evaluation of repeated electrowetting on three different fluoropolymer top coatings, *J. Micromech. Microeng.*, 2013, **23**(6), 067002.

27 B. Raj, M. Dhindsa, N. R. Smith, R. Laughlin and J. Heikenfeld, Ion and liquid dependent dielectric failure in electrowetting systems, *Langmuir*, 2009, **25**(20), 12387–12392.

28 L. X. Huang, B. Koo and C.-J. Kim, Sputtered–Anodized Ta2O3 as the Dielectric Layer for Electrowetting-on-Dielectric, *J. Microelectromech. Syst.*, 2013, **22**(2), 253–255.

29 M. G. Pollack, A. D. Shenderov and R. B. Fair, Electrowetting-based actuation of droplets for integrated microfluidics, *Lab Chip*, 2002, **2**(2), 96–101.

30 J. Gong and C.-J. Kim, Direct-referencing two-dimensional-array digital microfluidics using multilayer printed circuit board, *J. Microelectromech. Syst.*, 2008, **17**(2), 257–264.

31 K. Zhang, W. Wang, C. Li, A. Riaud and J. Zhou, 2D large-scale EWOD devices with honeycomb electrodes for multiplexed multidirectional driving of micro-droplets, *AIP Adv.*, 2020, **10**(5), 055227.

32 H. Ko, J. Lee, Y. Kim, B. Lee, C. H. Jung, J. H. Choi, O. S. Kwon and K. Shin, Active digital microfluidic paper chips with inkjet-printed patterned electrodes, *Adv. Mater.*, 2014, **26**(15), 2335–2340.

33 S. Naorungroj, S. Kin, S. Chun, S. H. Lee, O. S. Kwon, Q. L. Wang, E. H. Cho, C.-J. Kim, C. S. Henry, O. Chailapaku, N. Ngamrojanavanich and K. Shin, High-sensitivity electrochemical detection of HPV DNA via enzyme-amplified target-induced hairpin opening on a thermally controlled paper-based digital microfluidic platform, *Biosens. Bioelectron.*, 2025, 117898.

34 J. Li, N. S. Ha, T. Liu, R. M. van Dam and C.-J. Kim, Ionic-surfactant-mediated electro-dewetting for digital microfluidics, *Nature*, 2019, **572**(7770), 507–510.

35 J. Li and C.-J. Kim, *International Conference on Micro Electro Mechanical Systems (MEMS)*, Seoul, Korea (South), 2019.

36 S. Kalsi, S. L. Sellars, C. Turner, J. M. Sutton and H. Morgan, A programmable digital microfluidic assay for the simultaneous detection of multiple anti-microbial resistance genes, *Micromachines*, 2017, **8**(4), 111.

37 S. Anderson, B. Hadwen and C. Brown, Thin-film-transistor digital microfluidics for high value in vitro diagnostics at the point of need, *Lab Chip*, 2021, **21**(5), 962–975.

38 D. Wang, K. Jin, J. Ji, C. Hu, M. Du, Y. Belgaid, S. Shi, J. Li, S. Hu, A. Nathan, J. Yu and H. Ma, Active-matrix digital microfluidics design for field programmable high-throughput digitalized liquid handling, *iScience*, 2024, **27**(5), 109324.

39 Z. Jia, C. Jiang, J. Li, Y. Belgaid, M. Ge, L. Li, S. Hu, X. Huang, T. Y. Ho, W. Dong, Z. Yu and H. Ma, Intelligent single-cell manipulation: LLMs-and object detection-enhanced active-matrix digital microfluidics, *Microsyst. Nanoeng.*, 2025, **11**(1), 133.

40 X. Xie, Q. L. Wang, Y. Hu, R. Shi, T. Lei, C.-J. Kim and M. Wong, *International Conference on Solid-State Sensors, Actuators and Microsystems (Transducers)*, Florida, USA, 2025.

41 Q. L. Wang and C.-J. Kim, *International Conference on Micro Electro Mechanical Systems (MEMS)*, Kaohsiung, Taiwan, 2025.

42 W. Chu, H. Ji, Q. L. Wang, C.-J. Kim and A. L. Bertozzi, Electrohydrodynamics modeling of droplet actuation on a solid surface by surfactant-mediated electrodewetting, *Phys. Rev. Fluids*, 2023, **8**(7), 073701.

43 Q. L. Wang, P. Tian and C.-J. Kim, Surfactant-mediated electro-dewetting of droplets in oil for liquid-shape manipulation, *Droplet*, 2025, **4**, e70033.

44 M. J. Jebrail, R. F. Renzi, A. Sinha, J. Van De Vreugde, C. Gondhalekar, C. Ambriz, R. J. Meagher and S. S. Branda, A solvent replenishment solution for managing evaporation of biochemical reactions in air-matrix digital microfluidics devices, *Lab Chip*, 2015, **15**(1), 151–158.

45 H. C. Huang, C. C. Liang, Q. L. Wang, X. Huang, T. Y. Ho and C.-J. Kim, *Asia and South Pacific Design Automation Conference (ASP-DAC)*, Taipei, Taiwan, 2022.

46 Y. Pan, G. Liu, X. Huang, Z. Li, H. C. Huang, C. C. Liang, Q. Wang, C.-J. Kim and T. J. Ho, NR-Router+: Enhanced Non-Regular Electrode Routing With Optimal Pin Selection for Electrowetting-on-Dielectric Chips, *IEEE Transactions on*

Computer-Aided Design of Integrated Circuits and Systems, 2024, **43**(9), 2606–2619.

47 S. K. Fan, C. Hashi and C.-J. Kim, *International Conference on Micro Electro Mechanical Systems*, Kyoto, Japan, 2003.

48 H. Ma, S. Shi, K. Jin, D. Wang, S. Hu and Y. Su, *International Electron Devices Meeting (IEDM)*, San Francisco, CA, USA, 2020.

49 B. Hadwen, G. Broder, D. Morganti, A. Jacobs, C. Brown, J. R. Hector, Y. Kubota and H. Morgan, Programmable large area digital microfluidic array with integrated droplet sensing for bioassays, *Lab Chip*, 2012, **12**(18), 3305–3313.

50 J. Yu, S. Jiang, D. Wang, C. Chang, Z. Jia and M. Du, *International Electron Devices Meeting (IEDM)*, San Francisco, CA, USA, 2023.

51 S. Kalsi, M. Valiadi, M. N. Tsaloglou, L. Parry-Jones, A. Jacobs, R. Watson, C. Turner, R. Amos, B. Hadwen, J. Buse, C. Brown, M. Sutton and H. Morgan, Rapid and sensitive detection of antibiotic resistance on a programmable digital microfluidic platform, *Lab Chip*, 2015, **15**(14), 3065–3075.

52 D. Geng, K. Wang, L. Li, K. Myny, A. Nathan, J. Jang, Y. Kuo and M. Liu, Thin-film transistors for large-area electronics, *Nat. Electron.*, 2023, **6**(12), 963–972.

53 J. D. Sterling and C. Y. Chen, Keck Graduate Institute of Applied Life Sciences. Method, apparatus and article for microfluidic control via electrowetting, for chemical, biochemical and biological assays and the like, US 7163612B2, 2007, pp. 1–16.

54 S. Jiang, D. Wang, H. Ma, A. Nathan and J. Yu, Low temperature polysilicon pixel circuits for active-matrix digital microfluidic chips, *Displays*, 2025, **88**, 103048.

55 S. Zhan, R. Liu, Q. Luo, Y. Li, Y. Li, Z. Liu, M. Cheng and X. Cheng, Implementing AC Signal Driving in Digital Microfluidic Chips with Active-Matrix Thin-Film Transistors, *IEEE Sens. J.*, 2024, **24**(21), 33922–33928.

56 L. Lu, Z. Xia, J. Li, Z. Feng, S. Wang, H. S. Kwok and M. Wong, A comparative study on fluorination and oxidation of indium-gallium-zinc oxide thin-film transistors, *IEEE Electron Device Lett.*, 2017, **39**(2), 196–199.

57 H. Hosono and H. Kumomi, *Amorphous oxide semiconductors: IGZO and related materials for display and memory*, John Wiley & Sons, 2022.

58 T. H. Shih, H. C. Ting, C. L. Chen, L. Tsai, C. Y. Chen, L. F. Lin, H. S. Lin, L. H. Chang and Y. H. Lin, *International Workshop on Active-Matrix Flatpanel Displays and Devices (AM-FPD)*, Kyoto, Japan, 2014.

59 Z. Yang, K. Jin, Y. Chen, Q. Liu, H. Chen, S. Hu, Y. Wang, Z. Pan, F. Feng, M. Shi, H. Xie, H. Ma and H. Zhou, AM-DMF-SCP: integrated single-cell proteomics analysis on an active matrix digital microfluidic chip, *JACS Au*, 2024, **4**(5), 1811–1823.

60 Y. Hu, T. Lei, W. Jiang, Z. Zhang, Z. Xu and M. Wong, Spiking Neural Network Based on Memory Capacitors and Metal-Oxide Thin-Film Transistors, *IEEE Trans. Circuits Syst. II, Exp. Briefs*, 2024, 3965–3969.

61 Y. Hu, T. S. P. Ho, T. Lei, Z. Xia and M. Wong, Construction and Application of a Neuromorphic Circuit With Excitatory and Inhibitory Post-Synaptic Conduction Channels Implemented Using Dual-Gate Thin-Film Transistors, *IEEE Trans. Circuits Syst. I: Regul. Pap.*, 2024, 1582–1589.

62 X. Xie and M. Wong, *SID Symposium Digest of Technical Papers*, Wiley Online Library, 2025.

63 T. Lei, Y. Hu, X. Xie, R. Shi and M. Wong, In-Sensor Computing-Based Smart Sensing Architecture Implemented Using a Dual-Gate Meta-Oxide Thin-Film Transistor Technology, *Adv. Electron. Mater.*, 2024, 2400572.

64 T. Lei, Y. Hu, X. Xie and M. Wong, *International Conference on Solid-State Sensors, Actuators and Microsystems (Transducers)*, Kyoto, Japan, 2023.

65 X. Xie, K. Chen, Z. Zhou, W. Jiang, Y. Wang, S. Wang and M. Wong, *SID Symposium Digest of Technical Papers*, Wiley Online Library, 2023.

66 E. Hare and W. Zisman, Autophobic liquids and the properties of their adsorbed films, *J. Phys. Chem. B*, 1955, **59**(4), 335–340.

67 B. Bera, M. H. G. Duits, M. A. C. Stuart, D. Van Den Ende and F. Mugele, Surfactant induced autophobing, *Soft Matter*, 2016, **12**(20), 4562–4571.

68 J. Li, Y. Zhang, H. Fu, H. Yang, Y. Guan and Y. Zhang, *SID Symposium Digest of Technical Papers*, Wiley Online Library, 2023.